Chapter 4

Experimental Methods

The $Cu(In,Ga)Se_2$-based solar cell structure is complex and the fabrication involves several independent processing steps. The various processing steps are described in detail in this chapter. The detail of the growth process; single-stage, two-stage and three-stage processes used in the preparation of $Cu(In,Ga)Se_2$ absorber layers including with the *in situ* monitoring technique are described thereafter. The characterization techniques for the absorber films and solar cell devices are also reviewed in this chapter.

4.1 Fabrication of Ni-Al/ZnO/i-ZnO/CdS/$CuIn_{1-x}Ga_xSe_2$/ Mo/SLG Thin Film Solar Cells

The $Cu(In,Ga)Se_2$-based thin film solar cells is a heterojunction formed by a p-type chalcopyrite absorber layer and a transparent n-type window layer. Fig. 4.1 shows a schematic diagram of the typical structure of a $Cu(In,Ga)Se_2$-based thin film solar cell. Complete devices of this type studied in this work on the basis of MBD-grown $Cu(In,Ga)Se_2$ absorbers are built in a series of steps as shown in Fig. 4.2. After $Cu(In,Ga)Se_2$ deposition, the absorber film is covered with a thin CdS buffer layer. The solar cell device is then completed with the deposition of a ZnO window layer and Ni-Al grid front contacts. In this section, the fabrication processes are briefly outlined.

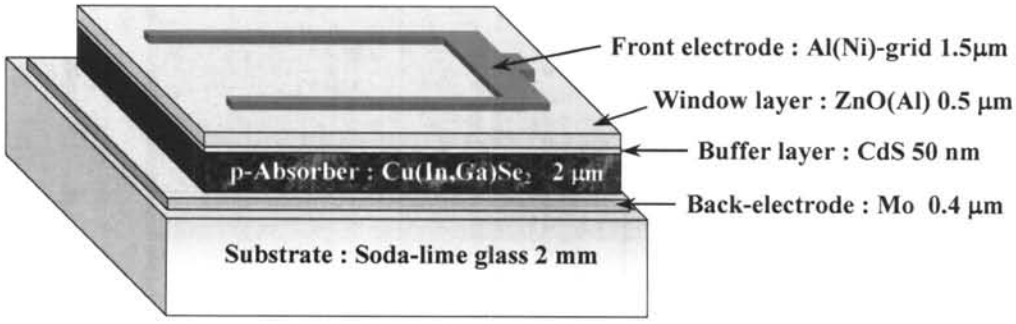

Figure 4.1: A schematic representation (not to scale) of $Cu(In,Ga)Se_2$-based thin film solar cell device.

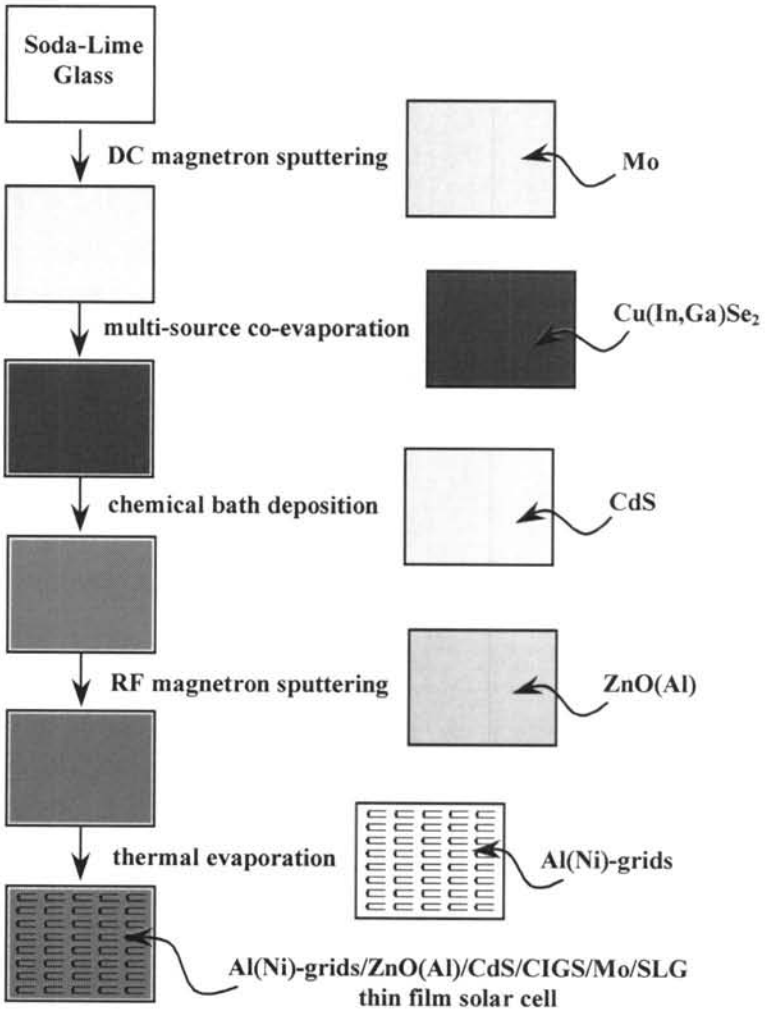

Figure 4.2: Processing steps of fabrication of $Cu(In,Ga)Se_2$-based thin film solar cell.

4.1.1 Substrate Preparation

All Cu(In,Ga)Se_2 thin films considered in this work were deposited on molybdenum coated soda-lime glass (SLG) substrates with the area of 3x3cm^2 and thickness of 2 mm. It provides beneficial that this polycrystalline material adheres well to the soda-lime glass. The SLG has advantages for use as substrates in $CuIn_{1-x}Ga_xSe_2$-based thin film solar cells because of matching thermal expansion coefficients, exhibition of a smooth surface, cheap and/or the diffusion of alkali metal from soda-lime glass into the layers [55]. The typical composition of SLG is given in Table 4.1 [56].

Table 4.1: Typical chemical composition of the soda-lime glass substrates.

Compound	SiO_2	Na_2O	CaO	MgO	K_2O	Al_2O_3	SO_3	Fe_2O_3
Content	72.2%	14.3%	6.4%	4.3%	1.2%	1.2%	0.3%	0.03%

Because the quality of the substrate prior to growth is a crucial factor which influences the properties of the deposited films. Surface defects such as scratches may have an adverse effect on the structural properties of films. In order to obtain clean substrates, the following procedure was routinely performed in our works:

Soda-lime glass substrates were cut and ultrasonically cleaned in a detergen (e.g. liquid soap) with temperature of 60°C for 30 minutes, then the samples were ultrasonically cleaned in deionized water with temperature of 60°C for 30 minutes several times. Finally, the glass substrates were blow dried with nitrogen gas. At least 8 samples were cleaned simultaneously and were kept under clean conditions until they were loaded into the MBE systems.

4.1.2 Molybdenum Back Contact Preparation

The first step of the fabrication process was the deposition of a thin (0.4 μm) molybdenum (Mo) layer on the SLG substrates using DC magnetron sputtering at room temperature with background pressure of $2x10^{-6}$ mbar. The sputtering of Mo films were performed at the argon pressure of about $5x10^{-3}$ mbar with a period of 10 minutes and the sputtered current of 1 A.

The Mo layer acts as the ohmic back contact to the cell. It is usually preferred because its thermal expansion coefficient is similar to that of SLG. Therefore, large stress gradients along the Mo/glass interface can be avoided after completion of the device. Such stress gradients might lead to a lower mechanical stability (adhesion) to the device. If the Mo layer is deposited under non-optimized conditions, it exhibits either tensile or compression stresses which contribute to the commonly observed peeling of $Cu(In,Ga)Se_2$ films at the Mo/$Cu(In,Ga)Se_2$ interfaces. Therefore, this will influence the electrical behavior of the absorber layer, as well as, solar cell devices.

4.1.3 $Cu(In,Ga)Se_2$ Absorber Layer Preparation

The key component of the $Cu(In,Ga)Se_2$-based thin film solar cells is the $Cu(In,Ga)Se_2$ absorber layer. The performance of cells are strongly influenced by structural properties of polycrystalline $Cu(In,Ga)Se_2$ layer such as composition, grain size, grain orientation and crystal defects. These properties affect to the energy loss mechanisms which, due to photo-generated carriers, recombine at the grain boundaries or the hetero-interfaces i.e., $Cu(In,Ga)Se_2$/Mo, CdS/$Cu(In,Ga)Se_2$. Moreover, phase segregation in $Cu(In,Ga)Se_2$ materials may also influence the transport mechanisms. The electrical and optical properties of $Cu(In,Ga)Se_2$ layers are dependent on their composition, defect chemistry and structure which in turn are

strongly related to the film growth parameters. The detail of preparation methods of these $Cu(In,Ga)Se_2$ polycrystalline absorber films are described in Section 4.2 and the material properties of the $CuIn_{1-x}Ga_xSe_2$ prepared using these methods are discussed Chapter 5.

4.1.4 Cadmium Sulfide Buffer Layer Preparation

Cadmium sulfide (CdS) has been used as the n-type semiconductor material to form the p-n junction with the p-type $Cu(In,Ga)Se_2$ absorber material. CdS has a direct band gap of 2.4 eV or an absorption edge at around 510 nm. Thus, some of lights in the blue region of visible solar spectrum are absorbed in the CdS layer and the carriers are generated which can also contribute to the total photo-generated current. The photons that have energy below 2.4 eV are transmitted through the CdS layer into the absorber layer.

A 50 nm thick CdS buffer layer was deposited on the $Cu(In,Ga)Se_2$ /Mo/SLG. The CdS buffer layer is a suitable layer in terms of crystal structure and electronic properties matching to the $Cu(In,Ga)Se_2$ absorber film. The CdS buffer layers were prepared by a chemical bath deposition (CBD) technique at temperature 60°C. The stock solutions of specific quantities (mole/volume) of cadmium sulfate ($CdSO_4$ with 0.004 mol/50cc), thiourea (NH_2CSNH_2 with 0.06 mol/cc) and ammonia solution (NH_3 with 4 mol/50cc) prepared at room temperature were used in our standard recipe for CBD-CdS technique. During the deposition time of about 10 minutes, the sample was shaken every minute. Immediately after the deposition, the sample was rinsed in de-ionized water and blown with nitrogen gas. The advantage of this technique is that complete surface coverage of the rough polycrystalline $Cu(In,Ga)Se_2$ films is obtained at low CdS thickness, typically 5-10 nm. Other technique such as evaporation require at least 1 μm thick for complete surface coverage. The CdS layer is deposited after the

absorber layers, and before the ZnO layer. The CdS will protect the absorber surface from the damage of ZnO-sputtering process. Therefore, the CdS has often been called "buffer layer".

4.1.5 ZnO(Al)/i-ZnO Window Bi-layer Preparation

The good window layer needs to satisfy two requirements. First, it has to be as transparent to the incident photons as possible, so that the photons can go through without absorption, to reach the $Cu(In,Ga)Se_2$ absorber layer. Secondly, the window layer has to be highly conductive, so that the photo-generated current can be easily conducted to external circuit. The sheet resistance of this layer should also be as low as possible because the current can easily flow to thin metal finger-grids which are separated by a significant distance between them. In the $Cu(In,Ga)Se_2$-solar cells the window layer is the bi-layer zinc oxide films. This bi-layer zinc oxide films consist of the zinc oxide (Al-doped), called "ZnO(Al)" and the intrinsic zinc oxide; i-ZnO layers. After finished the CBD-CdS process, the i-ZnO of about 500Å was first deposited by RF magnetron reactive sputtering at room temperature using Ar + 4 at% O_2. This was followed by a 4500 Å thick of ZnO(Al) layer prepared by RF magnetron sputtering from a 2.5wt% Al_2O_3-doped ZnO target.

4.1.6 Ni-Al Grid Front Contact Preparation

The solar cell device was completed by the evaporation of 2 μm thick Al grid contacts though a metal mask onto the ZnO window layer. The metallic grid mask used in this work was designed to give an individual cell with the total area of 0.50 cm^2, having 2.5% shading loss. In order to reduce resistive loss and prevent oxidation of Al, a 50 nm thick Ni layer was deposited before and after evaporation of Al layer. The thickness of each layer was monitored by using an oscillating quartz crystal

monitor. Finally, cell areas were delineated by mechanical scribing to produce individual cells with 0.5 cm^2 area shown in Fig 4.3.

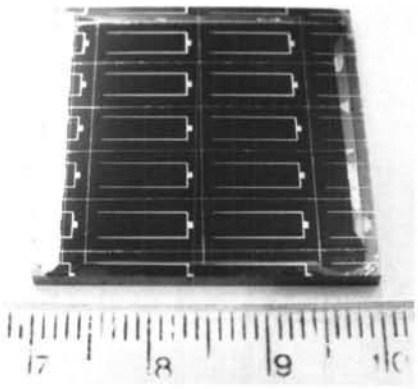

Figure 4.3: Photograph of $Cu(In,Ga)Se_2$-based thin film solar cells 10 cells fabricated at SPRL.

4.2 Preparation of $Cu(In,Ga)Se_2$ Thin Films

It should be noted that, although the major part of this work dealt with the growth process of wide band gap $Cu(In,Ga)Se_2$ absorber layer, it start out with optimization of our (regular) $Cu(In,Ga)Se_2$ absorber growth process. In this work, various parameters for the absorber deposition were changed from time to time. Most of these films were prepared using MBD with *in situ* monitoring technique. However, this technique was divided into two-stage and three-stage growth processes, respectively. By using the *in situ* monitoring technique, we can predict when the growth process has been finished (end point detection) and the desired composition of films can be obtained.

In this section, we start with the detail of the growth process of $Cu(In,Ga)Se_2$ absorber layer followed by the *in situ* monitoring and end point detection technique.

4.2.1 Two-stage Growth Process

The two-stage growth process generally called "bilayer process" or "Boeing recipe". The temperature profiles of effusion cells and substrate are shown in Fig 4.6. There are two following features of this two-stage process:

(i) effusion cell temperatures and substrate temperature are constant,

(ii) all of the Cu flux is deposited prior to t_1. Thus the thickness of Cu, d_{Cu}, can be written as

$$d_{Cu}(t_1) = d_{Cu}(t_2), \tag{4.1}$$

where $d_i(t)$ is the film thickness of metal i at time t.

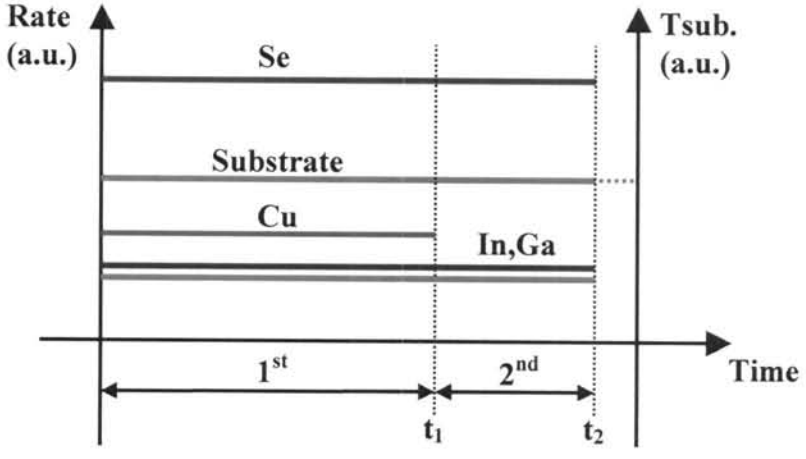

Figure 4.4: Temperature profiles of two-stage growth process.

According to the fact that at constant effusion cell temperature, the thickness d_i is proportional to the deposition rate of element i; r_i, and the deposition time t_i. Thus

$$d_i = r_i \cdot t_i . \tag{4.2}$$

The relations of the corresponding deposition rate of Ga and In can be written as (see detail in appendix B),

$$r_{Ga} = \frac{x}{y} \cdot \frac{\alpha_{Cu}}{\alpha_{Ga}} \cdot r_{Cu}, \qquad (4.3A)$$

and

$$r_{In} = \frac{(1-x)}{y} \cdot \frac{\alpha_{Cu}}{\alpha_{Ga}} \cdot r_{Cu}, \qquad (4.3B)$$

where α_i is the parameter defined as following:

$$\alpha_{Cu} = \rho_{Cu} \cdot M_{Cu}^{-1},$$

$$\alpha_{In} = \rho_{In} \cdot M_{In}^{-1},$$

$$\alpha_{Ga} = \rho_{Ga} \cdot M_{Ga}^{-1},$$

ρ_i is the density of the metal i, M_i is the mass per mole of the metal i.

Substitute Eqs. 4.2 and 4.3a into Eq. 4.1, we obtain

$$\frac{y(t_1)}{x} \cdot \frac{\alpha_{Ga}}{\alpha_{Cu}} \cdot r_{Ga}(t_1) \cdot t_1 = \frac{y(t_2)}{x} \cdot \frac{\alpha_{Ga}}{\alpha_{Cu}} \cdot r_{Ga}(t_2) \cdot t_2. \qquad (4.4)$$

Since all effusion cells temperature are constant, so the deposition rate of Ga (r_{Ga}) is constant during the growth process; $r_{Ga}(t_1) = r_{Ga}(t_2)$, thus Eq. 4.4 can be written as

$$y(t) = \frac{y(t_1)}{t} \cdot t_1 \qquad \text{for } t \geq t_1, \qquad (4.5)$$

where $y(t_1) \cdot t_1 = y(t_2) \cdot t_2$.

From Eq. 4.5, the evolution of the compositions of film, y(t) and x(t) is shown in Fig. 4.5.

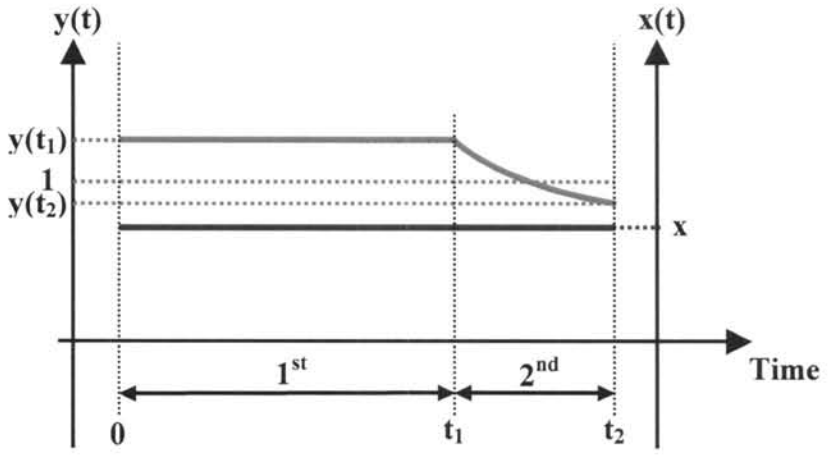

Figure 4.5: Evolution of composition in two-stage growth process.

Figure 4.4 and 4.5 show that the process starts with the growth of Cu-rich film ([Cu]/([In]+[Ga]) >1; y>1) in the first stage while all effusion cell temperatures are kept constants. At the end of the first stage (at $t = t_1$), the Cu effusion cell is turned off. In the second stage, the Cu-content, y, of the growing film decreases from Cu-rich to Cu-poor composition. At the end of the growth process (at $t = t_2$), the final desired composition, $y(t_2)$, can be obtained by using the *in situ* monitoring signals. During the growth process, the Ga-content, x, of the growing film is kept constant. The temperature of substrate (T_{sub}) and effusion cell-Se temperature (T_{Se}) are chosen at some values, which depend on film quality and compositional requirements (e.g. T_{sub} is controlled at 520°C and T_{Se} at 190°C). The detail of the calculation of growth parameter is shown in the appendix B.

4.2.2 Three-stage Growth Process

The most efficient $Cu(In,Ga)Se_2$ solar cells to date were obtained with absorbers grown with the three-stage process [57, 58, 59]. First, an $(In,Ga)_2Se_3$ precursor layer is deposited at low substrate temperature (300-350°C). In the second stage, Cu and Se

are co-deposited at a higher substrate temperature (typically 530°C) until the overall composition becomes Cu rich. In the third stage, In order to obtain a Cu-poor composition absorber film, where the ratio [Cu]/([In]+[Ga])<1, a small amount of In, Ga and Se are co-evaporated at still the same substrate temperature until the required overall Cu deficiency of the film is reached.

The temperature profile of the $Cu(In,Ga)Se_2$ three-stage growth process in our work is shown in Fig. 4.6. In the initial growth within the time t_{1a}, y=0 due to no Cu flux. In the 2nd stage ($t > t_{1a}$) the shutter of Cu effusion cells is opened, the r_{Cu} increases and the film becomes Cu-rich at the end of 2nd stage. At $t = t_1$, the shutter of Cu effusion cells is turned off. Therefore, the Cu-content, y, of the growing film decreases from Cu-rich to Cu-poor (see Fig. 4.7).

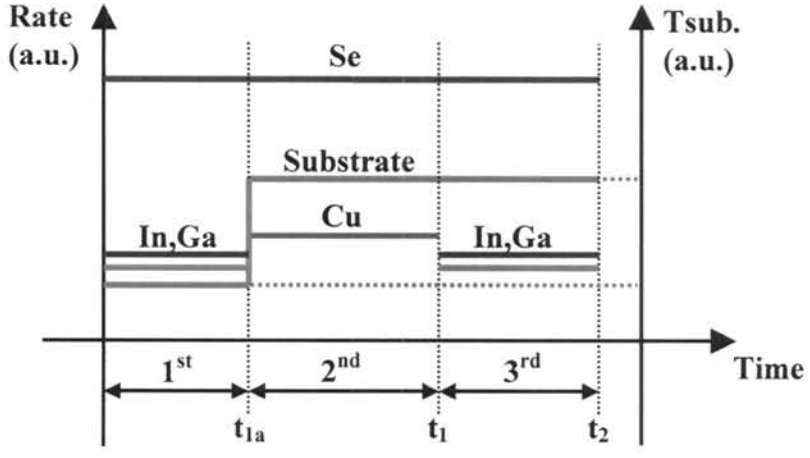

Figure 4.6: Temperature profiles of three-stage growth process.

The Cu-content in the three-stage growth process can be calculated similar to Section 4.2.1. In this growth process, the relation between t_{1a}, t_1 and t_2 can be written as

$$d_{Cu}(t_1 - t_{1a}) = d_{Cu}(t_1) = d_{Cu}(t_2). \qquad (4.6)$$

Substitute Eqs. 4.2 and 4.3A into Eq. 4.6, we obtain (see detail in the appendix B)

$$y(t_1 - t_{1a}) \cdot (t_1 - t_{1a}) = y(t_1) \cdot t_1 = y(t_2) \cdot t_2 . \qquad (4.7)$$

Thus, the important expression between Cu-content and deposition time in the three-stage growth process can be expressed as

$$y(t) = \frac{y(t_1 - t_{1a}) \cdot (t - t_{1a})}{t} \qquad \text{for } t_{1a} \le t \le t_1, \qquad (4.8)$$

and

$$y(t) = \frac{y(t_1)}{t} \cdot t_1 \qquad \text{for } t \ge t_1. \qquad (4.9)$$

From Eq. 4.9 and Fig. 4.6, the evolution of film composition y(t) and x(t) is shown in Fig. 4.7.

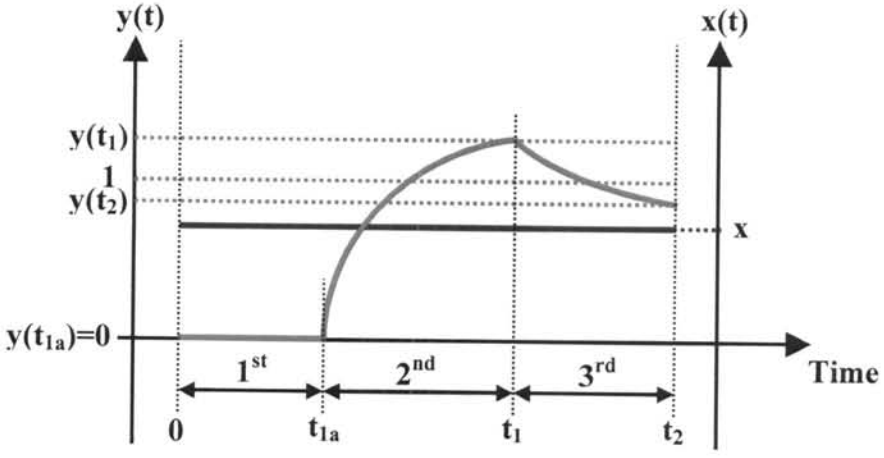

Figure 4.7: Evolution of composition in three-stage growth process.

4.2.3 *In situ* Monitoring and the End Point Detection Technique

In this work, we use the *in situ* monitoring technique combines with the two-stage or three-stage Cu(In,Ga)Se_2 growth process. The *in situ* signals consists of (i) the

temperature of the surface of substrate read using pyrometer (T_{pyro}), (ii) the output power of substrate temperature controller (OP).

The substrate was directly heated up by radiation through the sapphire diffuser from a Ta heater. The substrate temperature was controlled and kept constant by regulating the output power (OP) of the temperature controller using feedback signal from the thermocouple above the back of the substrate. The thermal radiation from the front surface of the substrate was monitored by the pyrometer. During growth process, the substrate temperature (T_{sub}), OP and T_{pyro} were monitored simultaneously.

End point detection is an *in situ* method to predict when the growth process is finished. T. Nishitani *et al.* [60] described in 1995 a method to detect the transition from a Cu-poor to Cu-rich film or vice versa. The method becomes known as "end-point detection" (EPD). It is based on the emissivity of Cu-rich film is higher than the emissivity of stoichiometric or Cu-poor film. For example, when the phase transition from Cu-rich to Cu-poor composition in the second stage of two-stage process occurred, the surface will dissipate less heat by radiation. Thus, the temperature of the substrate will increase. Since the substrate heater is PID controlled, with feedback from the thermocouple behind the substrate, to have constant temperature the power consumption of the substrate heater will decrease as shown in Fig 4.8.

Typically, in the first stage of both two-stage and three-stage growth process, the pyrometer signal intensity oscillates with progressing process time. The reflection of black body radiation at the back and front surfaces of the growing film leads to interference and therewith the pyrometer signal oscillation is a measure of the film growth rate. The relationship between the thickness and the interference oscillation period was consistent. The maximum and minimum points could roughly be calculated by the following equations;

$$\text{Maxima: } (2m+1)\,\lambda/4 = nd\,,\ (m= 0,1,2,\ldots) \qquad (4.10)$$

$$\text{Minima: } (2m+2)\,\lambda/4 = nd\,, \qquad (4.11)$$

where n is the refractive index, λ is the monitoring wavelength, and d is the thickness.

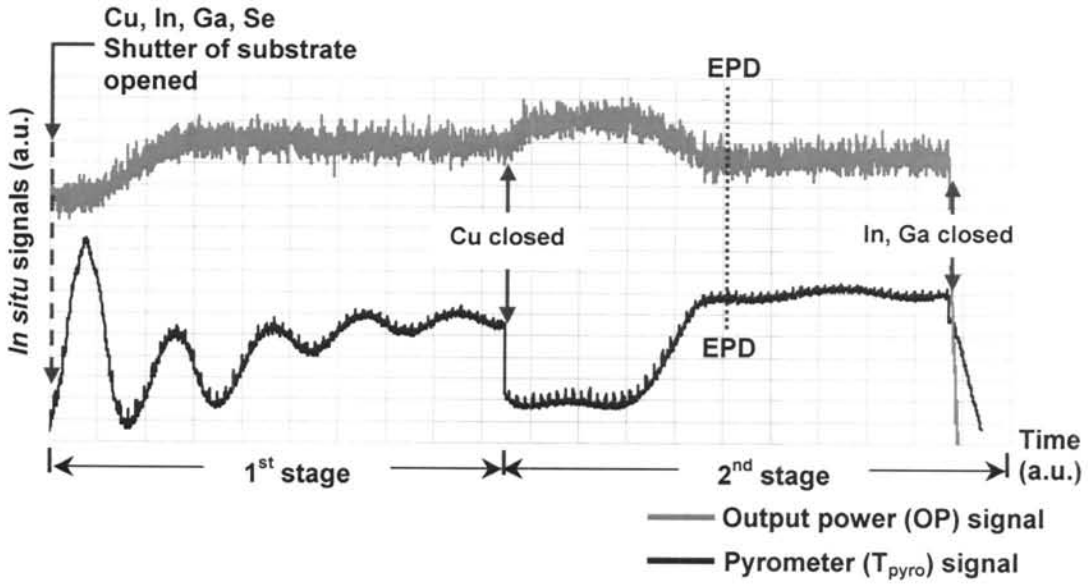

Figure 4.8: *in situ* monitoring signals of the $CuIn_{1-x}Ga_xSe_2$ film grown with the two-stage as a function of process time.

The pyrometer signal shows the amplitude of oscillation decreasing with the deposition time. This is due to the decrease of the transmittance of the IR radiation through the substrate as the film thickness is increasing.

Figure 4.10 shows the example of the typical *in situ* monitoring signals of two-stage growth process as a function of process time. This can be explained as the following. In the 1st stage, when the shutter of all effusion cells and shutter of substrate is opened, the growth process begins. A sudden jump of the T_{pyro} at the beginning of the process is due to the exposure of the substrate to the hot sources. When the Cu-rich film starts to grow, the T_{pyro} rapidly increases to a certain value and then decreases to become a sharp peak which is followed by several periods of

oscillations. This sharp peak and the oscillations of T_{pyro} are the result of the optical interference of the 1.55 μm radiation by thin film which is detected by the pyrometer. Because of the poor transparency of the film at this wavelength, the amplitude of interference decrease as the thickness of the film increases. At large thickness of film, the T_{pyro} shows a certain equilibrium at the end of 1st stage ($t = t_1$). However, during this sage, when the Cu-rich film starts to grow on the front surface, the substrate temperature which is detected using thermocouple slightly decrease. The decrease in the substrate temperature is caused by the increase of the emissivity of the Cu-rich film. Then the output power of the temperature controller (OP) must increase in order to keep the temperature of the substrate constant. This is clearly observed from the OP monitoring signal.

At the 2nd stage, when the shutter of Cu effusion cell is closed, reflected from the Cu source reaching the substrate decrease accordingly. The T_{pyro} shows a sudden drop to a certain value. The growth of the $Cu(In,Ga)Se_2$ film without Cu flux in this stage is solely achieved by In, Ga and Se fluxes. In this stage, the transition of the Cu-rich film to Cu-poor composition film occurred, one would expect the decrease in the emissivity of the surface and the rise in the surface temperature. This effect can be observed by the increase of the T_{pyro} signal, thus, cause a decrease of the output power supplied to the substrate heater. The decrease of this output power is shown by the decrease of the OP signal together with the sharp corner and the flat plateau of the Cu-poor film. Both sharp knees of the T_{pyro} and OP signals occur at the same position of the time scale. We attribute these transitions of both monitoring curves to the point indicating that the $Cu(In,Ga)Se_2$ film has been completely transformed to the Cu-poor composition. Thus, we may assign this point to be the end point for the growth process.

4.3 Characterization of $Cu(In,Ga)Se_2$ Thin Films

In this work, several of characterization techniques were used to evaluate the material quality of the films. The structural properties of the polycrystalline $Cu(In,Ga)Se_2$ thin films were studied by scanning electron microscopy (SEM) and the presence of crystalline phases by X-ray diffraction (XRD). The compositions were determined by energy dispersive X-ray spectroscopy (EDS). The morphology of films was observed by atomic force microscopy (AFM). The optical properties of the films were evaluated by UV-VIS-NIR spectrophotometer. Completed devices were evaluated in the dark and illumination by standard I-V characterization equipment. The most important features of these characterization techniques are outlined in the following sections.

4.3.1 Structural Analysis

In this section, the techniques used for the structural and/or compositional characterization of $Cu(In,Ga)Se_2$ films and related devices will be reviewed. They include the scanning electron microscopy, electron microprobe for energy dispersive X-ray analysis and atomic force microscopy.

Scanning Electron Microscopy (SEM)

In this work, the morphology and composition of $Cu(In,Ga)Se_2$ films were characterized using SEM equipped with EDS. The SEM micrographs were carried out from LEO 1455 system. SEMs often have a microprobe for energy dispersive analysis by studying the characteristic X-ray lines for rapid evaluation of elemental constituents.

The characteristic X-ray emitted from $CuIn_{1-x}Ga_xSe_2$ thin film when bombarded by focused electron beam on a small area of sample surface can be measured in EDS mode in SEM system. Generally, the EDS has an effective probe depth of ~ 1 μm, and may be limited to detection of elements with Z>11 due to the use of a Beryllium window at the detector. In this work, the EDS is performed for acceleration voltages of 25 kV. A typical X-ray spectrum from EDS measurement of our $Cu(In,Ga)Se_2$ thin film is shown in Fig. 4.9.

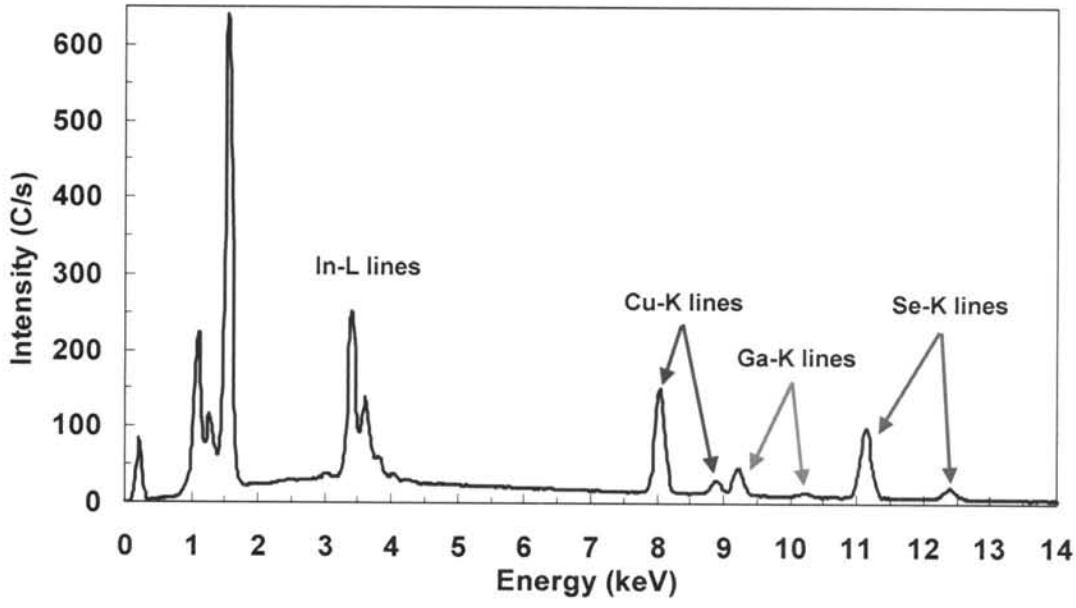

Figure 4.9: X-ray spectrum of a $Cu(In,Ga)Se_2$ thin film.

The distributions of X-ray intensities at the peaks of Cu, In, Ga and Se can be determined by the peak-fitting method. This method is able to figure and identify the X-ray of the elements in the sample and also can deduce the atomic weight percent of

Cu, In, Ga and Se of $Cu(In,Ga)Se_2$ samples. Hence, the atomic compositions of $Cu(In,Ga)Se_2$ thin film can be determined.

The peaks of Cu-K lines, In-L lines, Ga-K lines and Se-K lines in the X-ray spectrum were chosen and fitted by using the Gaussian function (G);

$$G = I \times \exp\left[-0.5 \times \left(\frac{E - C}{W} \right)^2 \right], \tag{4.12}$$

and

$$W = \frac{FWHM}{2\sqrt{2\ln 2}}, \tag{4.13}$$

where I is the amplitude of the peak, E is the energy, C is the energy at the center of peak, and W is the width of peak calculated using Eq. 4.13, and FWHM is the full width at half maximum of the peak.

Then by integrated Eq. 4.12, we obtain the peak area

$$A = \int_{-\infty}^{+\infty} I \times \exp\left[-0.5 \times \left(\frac{E - C}{W} \right)^2 \right] dE, \tag{4.14}$$

$$A = I \times W \times \sqrt{2\pi}\,. \tag{4.15}$$

The background intensity of the spectrum was fitted using quadratic function of X-ray energy. Then, it was subtracted from the spectrum giving only the characteristic X-rays of each element in the spectrum. After that, the characteristic X-rays of each peak were fitted to Gaussian function by using Eq. 4.12. Finally, the peak area can be obtained by Eq. (4.15). The peak area of this $Cu(In,Ga)Se_2$ standard sample will be used as standard for normalized peak area of typical X-ray spectrum of $Cu(In,Ga)Se_2$ thin films. The normalized peak area of each peak can be calculated for the atomic weight percent of Cu, In, Ga and Se including the ratios of [Cu]/([In]+[Ga]) and [Ga]/([In]+[Ga]).

Atomic Force Microscopy (AFM)

The atomic force microscope is one type of scanned- proximity probe which is used to measure various local properties of the sample, such as height, roughness, and grain size. AFM system consists of a tube-scanner, a position-sensitive photo detector and the cantilever with a probe located at the free end. The cantilever bends in response to the interaction force between the tip and sample.

In principle, during the probe scan across the surface of the sample, a constant force between the tip and the sample is maintained. As the cantilever deflects caused by changes in surface topography, the light from the laser is reflected onto the split photodiode. By measuring the signal difference of A-B as shown in Fig 4.10, the bending of the cantilever can be measured and used to generate a map of surface topography.

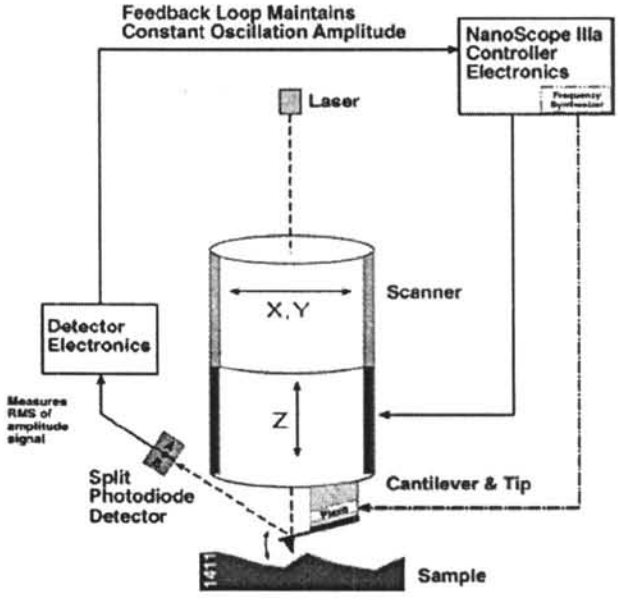

Figure 4.10: Working principle of the AFM (non contact tapping mode).

The surface roughness determined by the AFM is the root mean square (rms) roughness, z_{rms}, which is defined as

$$z_{rms} = \sqrt{\sum_i \frac{(z_i - \bar{z})^2}{N}}, \qquad (4.16)$$

where $\bar{z}$ is the average height of the scanned area, z is the height value of each point and N is the number of the points including the scanned area.

X-ray Diffraction Technique (XRD)

X-ray diffraction is a non-destructive technique to identify the crystalline phases present and analyze the structure properties. In this study, we use a Bruker model D8 X-ray diffractrometer and Cu Kα radiation with wavelength of 1.5418 Å with 30kV, 20mA. The XRD spectra were collected in the 20° – 80° of 2θ range with a measurement step of 0.02° for most samples in order to carry out phase analysis.

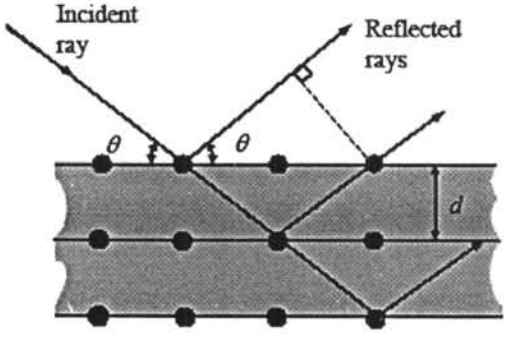

Figure 4.11: Diffraction of X-rays from parallel planes in the crystal.

Identification of the phases from XRD was done using Bragg's law:

$$2d\sin\theta = n\lambda, \qquad (4.17)$$

where d is the interplanar spacing, θ the Bragg angle and λ the wavelength of X-rays. In the case of the tetragonal system, to which most of the samples encountered in this work;

$$\frac{1}{d^2} = \frac{h^2 + k^2}{a^2} + \frac{l^2}{c^2}, \qquad (4.18)$$

and $$d = \frac{ac}{\sqrt{c^2(h^2 + k^2) + a^2 l^2}}, \qquad (4.19)$$

where h, k, l are the Miller indicies of the diffraction planes, and a and c are lattice parameters. The crystalline phases were identified by matching the experimentally measured XRD peak positions with those given in the Joint Council for Powder Diffraction Studies (JCPDS) files. A typical XRD pattern of $Cu(In,Ga)Se_2$ thin film grown by MBD using two-stage process is shown in Fig. 4.12.

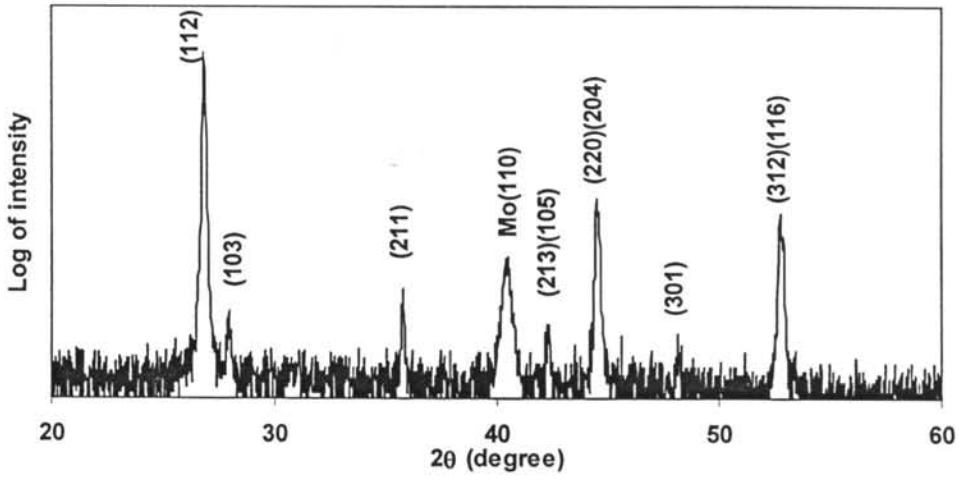

Figure 4.12: Typical XRD spectrum of the $Cu(In,Ga)Se_2$ thin films.

4.3.2 Transmittance and Reflectance Measurements

In this work, the transmittance and reflectance spectra were measured with a Perkin Elmer Lambda 900 spectrometer. It is a total reflective double-beam spectrometer. The working spectral range is from 300 nm to 2600 nm (for transmittance), covering the ultra-violet (UV), visible and near-infrared (IR) spectrum. For UV radiation the deuterium lamp is used and halogen lamp gives off visible and IR radiation. The $Cu(In,Ga)Se_2$ sides of the samples were irradiated under perpendicular angle of

incidence while the reference used was SLG and standard mirror for transmission and reflection measurement, respectively.

The optical transmission (T) of a transmitting medium is defined as the ratio of the intensity of transmitted radiation to that of the incident radiation, I/I_0. These two intensities are related to the absorption coefficient (α), and the path length or film thickness (d) by the expression:

$$I = I_0 e^{-\alpha d}. \tag{4.20}$$

By taking reflection into account, for an incident intensity I_0 at the front surface, the transmitted radiation is given by $(1\text{-}R)I_0$, where R is the optical reflection. Thus, the radiation reaching the back surface is $(1-R)I_0 e^{-\alpha d}$. By taking the multiple reflections into account, the total transmitted radiation can be expressed as [61]

$$T = \frac{I}{I_0} = \frac{(1-R)^2 e^{-\alpha d}}{1-R^2 e^{-2\alpha d}}, \tag{4.21}$$

4.3.3 Current-Voltage (I-V) Characterization

The device performances were measured under standard test condition (AM 1.5, 25°C) using a typical solar simulator based on a single 300W-ELH lamp (tungsten-halogen light source), normalized to a light intensity of 100 mW/cm^2 as illustrated in Fig. 4.13. The device sample was placed on a temperature controlled stage (25 ± 2°C) and contacted with two-point probe configuration. A Keithley model 238 was used as current source and voltage measurement. These signals were real-time accessed to display on a PC via IEEE-488 interface card and the parameters of cell characteristics (e.g. series resistance R_S, shunt resistance R_{SH}, open-circuit voltage V_{OC}, short-circuit current density J_{SC}, fill factor FF and efficiency η) can be determined as described in detail in Section 2.4.3.

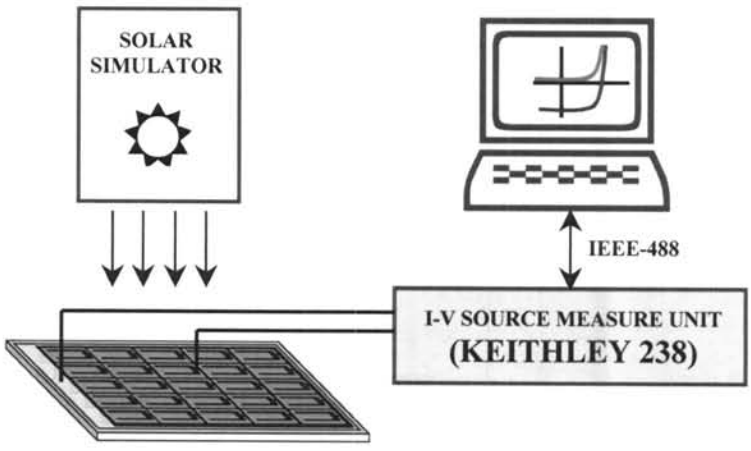

Figure 4.13: Schematic diagram of the I-V measurement system.